




# Earth's Outgoing Radiation Monitoring From the Moon

Jing Huang, Huadong Guo , *Member, IEEE*, Guang Liu , and Hanlin Ye 

**Abstract**—Earth's outgoing radiation (EOR) at the top-of-atmosphere (TOA) is a vital parameter of earth's energy budget. Moon-based earth observations as one of the scientific goals of the International Lunar Research Station (ILRS) project could provide long-term, well-calibrated, and disk-integrated EOR data to complement existing platforms. To study the difference between a Moon-based platform and existing platforms, in this study, we established a method to simulate outgoing longwave (OLR) and shortwave radiation (OSR) from a Moon-based radiometer. Then, by parameterizing Moon-based earth observations, the relationship between observation geometry and diurnal and seasonal variations of OLR were derived. Finally, the relationship between OSR viewed from a Moon-based sensor and earth's phase is obtained. We summarized three Moon-based EOR observation characteristics. 1) Moon-based observational scope is almost earth's hemisphere, and Earth–Moon distance has great effects on EOR. With the Moon moves from perigee to apogee, the OLR decreases almost 40% and OSR decreases about 60%. 2) Diurnal and seasonal variations also influent OLR, and compared correlation coefficients between OLR removing the effects of seasonal with diurnal, the former has bigger value, meaning hemisphere-scale observations is less sensitive to seasonal signals. 3) A Moon-based platform can observe the earth with different earth's phases. For OLR, earth's phase changes earth's scene. For OSR, with the increase of earth's phase, OSR is greatly decreased, the ratio of incoming shortwave radiation (ISR) is close to earth albedo when the earth's phase is 0°. Our results offer new understanding that will help to facilitate Moon-based monitoring of EOR.

**Index Terms**—Analysis, earth's outgoing radiation, moon-based platform, numerical simulation.

## I. INTRODUCTION

**E**ARTH system science emphasizes a holistic view of the dynamic interaction between earth's spheres [1], [2], [3]. One of the most important problems in earth system science is earth's

radiation budget, which consists of incoming solar radiation (ISR), longwave radiation (LW) emitted by the earth's surface and atmosphere, and reflected of solar radiation (i.e., shortwave radiation, SW), which determine the radiation balance of the earth system [4], [5], [6], [7]. Fundamental requirements for earth radiation data are acquisition at a global scale, unbiased measurements, absolute calibration accuracy, and sufficient spatial and temporal resolution.

Significant efforts have been made to accurately measure both top-of-atmosphere (TOA) LW and SW using space-borne platforms [8], [9], [10]. In the 1960s and 1970s, Nimbus 6 and 7 were equipped a narrow (NFOV) and wide field of view (WFOV) instruments to measure earth's outgoing radiation (EOR) [11]. The field of view of a WFOV radiometer is several thousand kilometers, while the spatial resolutions of NFOVs reach 10 to 100 km. Since NFOV instruments do not directly measure a flux, angular distribution models (ADMs) are used to convert the radiance to flux [12]. In the 1980s, new generation devices were developed, including the earth radiation budget experiment (ERBE) instruments onboard three satellites to measure SW and LW radiances [13], [14]. This was the first approach to include the cloud factor, which has a cooling effect in EOR determination. The clouds and the earth's radiant energy system (CERES) experiment enabled real-time tracking of earth's radiation by measuring TOA SW and LW; moreover, it clearly linked cloud effects to global climate change [9], [15], [16]. For example, from earthshine data from 1998 to 2017, scientists found the albedo declines about 0.5 W/m<sup>2</sup>. Compatible with CERES and MODIS data, they found out the sky over eastern Pacific were bright and covered with noticeable less cloud which causes the decrease in albedo. To achieve high measurement accuracy, these instruments are calibrated both in-flight and on the ground [17], [18]. Compared with the instruments of early measurements, each provides higher spatial resolution, longer time records, and increased accuracy [9], [10], [19]. For a better understanding of the diurnal variation of EOR, the geostationary earth radiation budget (GERB) was developed to produce a global image (excluding areas poleward of 72°) every 15 mins [20]. As with CERES, measurements from GERB instruments are paired with cloud retrievals from the Spinning Enhanced Visible and Infra-Red Imager (SEVIRI). In China, the measurement of EOR is a major mission of the Feng Yun (FY)-3 series. The instruments onboard FY-3 can observe earth-reflected solar SW and earth-emitted LW radiances [21]. This is an attempt to observe the EOR from polar-orbiting meteorological satellites. Since 2015, the Deep Space Climate Observatory (DSCOVR) has given a

Manuscript received 8 June 2022; revised 31 July 2022 and 30 August 2022; accepted 31 August 2022. Date of publication 7 September 2022; date of current version 21 September 2022. This work was supported in part by the National Key Research and Development Program of China under Grant 2020YFE0202100, in part by The Key Research Program of Frontier Sciences, CAS under Grant QYZDY-SSW-DQC026, and in part by the National Natural Science Foundation of China under Grant 42101413. (*Corresponding author: Guang Liu.*)

Jing Huang, Huadong Guo, and Guang Liu are with the Aerospace Information Research Institute, Chinese Academy of Sciences, Beijing 100094, China, also with the University of Chinese Academy of Sciences, Beijing 100049, China, and also with the International Research Center of Big Data for Sustainable Development Goals, Beijing 100094, China (e-mail: huangjing@radi.ac.cn; hdguo@radi.ac.cn; liuguang@radi.ac.cn).

Hanlin Ye is with the Qian Xuesen Laboratory of Space Technology, China Academy of Space Technology, Beijing 100094, China (e-mail: ye hl@radi.ac.cn).

Digital Object Identifier 10.1109/JSTARS.2022.3204850

new perspective for earth observation [22], [23] as it observes the whole disk sunlit part of the earth at Lissajous 1 orbit [24]. NIST Advanced Radiometer onboard DSCOVR is the most advanced sensor to detect earth outgoing radiation, which has same hemisphere-scale scope as a Moon-based platform, its observation accuracy can reach to 0.1%–1.5% (varies with band).

Throughout the development of EOR observations, the general tendency has been to achieve higher accuracy of measurements. To achieve this goal, one method is to reduce the calibration errors of the sensors [25]. Another is to realize global observations as much as possible, such as enlarging the observational scope by using constellations of small satellites [26], [27].

In addition to using artificial space-borne platforms, observations from the Moon could also become an important part of earth radiation budget monitoring. Observing the earth from a Moon-based platform would offer a unique dataset [1]. First, owing to tidal locking and the large earth–Moon distance, a Moon-based sensor would simultaneously acquire critical parameters with hemisphere observations. Second, the lunar surface has abundant space. Some scholars have investigated suitable locations to place earth observation sensors and how the lunar surface environment would affect those sensors [28], [29]. By combining various sensors, such a system would be able to simultaneously measure parameters ranging from the subsurface to the plasmasphere. Third, unique lunar orbit brings various observational angles. For mid–low earth latitudes, a Moon-based platform could realize long-term observations lasting for  $\sim 10$  h [30]. Measuring the parameters of earth's radiation budget requires the angular characteristics of radiation. Various angular sampling could supplement existing earth observations, and would help to improve retrieval accuracy [30]. These peculiarities make EOR measured by a Moon-based platform different. For the Moon-based earth observations, its observational scope is almost earth's hemisphere including various mixed scene types and changing inclination of lunar orbit brings various observational angles from different directions for one point on the earth surface, radiation observed by a Moon-based platform is integrated by elements. For CERES, its observational scope is much smaller than a Moon-based platform and observational angle is in fixed direction. For hemisphere EOR, CERES data should be obtained by stitching satellite data. In summary, a Moon-based platform could acquire large-scale observations and complement existing earth observations.

To evaluate the potential radiation measurement capacity of a prospective Moon-based active cavity radiometer, it is necessary to simulate the outgoing longwave radiation (OLR) and outgoing shortwave radiation (OSR) observed at the entrance pupil of the radiometer. At present, although many studies have considered Moon-based earth observation geometry, a method for simulating Moon-based radiation monitoring of EOR is still needed. As the positions of lunar orbit changes, observed EOR at the entrance pupil would also change. This article mainly answers the question that what characteristics for Moon-based EOR observations, and compared to existing satellites, what are its peculiarities. We present a method for simulating the observed OLR and OSR at the entrance pupil of a Moon-based

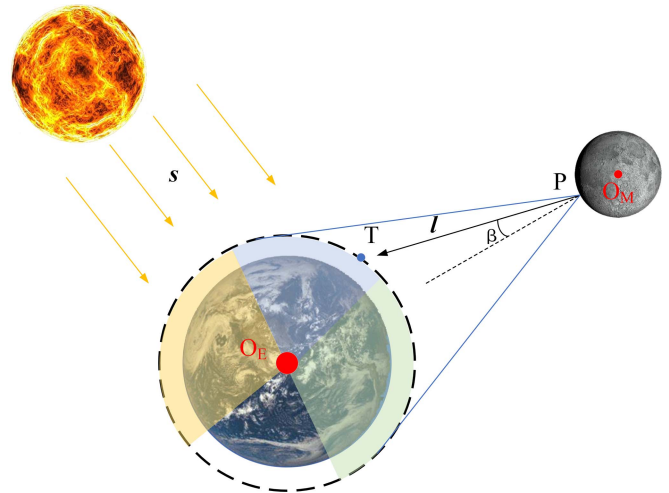


Fig. 1. Schematic of Moon-based earth observations. The blue-shaded zone shows the sector that is both sunlit and could be observed by a Moon-based sensor (also known as the earth's phase).

radiometer as a function of changing orbit. This study makes three main contributions. First is the establishment of a method to simulate OLR and OSR at the entrance pupil of a Moon-based radiometer. The second is the parameterization of Moon-based earth observations and identification of the relationship between observation geometry and diurnal and seasonal variations in observed earth OLR. The third is to contact OSR with earth's phase, through the OSR within a Moon-based platform scope and ISR, the ratio between them is obtained.

## II. PROBLEM STATEMENT AND MODEL ANALYSIS

The objectives of this article were to simulate the OLR and OSR received by a Moon-based active cavity radiometer. This required parameterization of Moon-based earth observation geometry and an analytical method for observing the earth disk as a single measurement.

### A. Moon-Based Earth Observation Geometrical Model Parameterization

Detailed transformation of the earth and Moon to the same coordinate systems is shown in [31]. There are eight main coordinate systems involved in this transformation. Fig. 1 shows a schematic of Moon-based earth observations, where  $O_M$  and  $O_E$  are barycenters of the Moon and the earth, and  $R_m$  is the radius of the Moon. Point P on the lunar surface represents the position of the Moon-based sensor. Point T is the observed point on the TOA of the earth within the observational scope. The vector  $l$  is the light ray from the earth's position T to the entrance pupil of the Moon-based radiometer.

Denoting the Moon-based platform's position in the body-centered body-fixed coordinate system  $\mathbf{p}_{\text{MCMF}}$ , the position in the International Terrestrial Reference System (ITRS) can be written as

$$\mathbf{p}_{\text{ITRS}} = [\Theta][\mathbf{I}][\mathbf{N}][\mathbf{P}][\mathbf{B}][\mathbf{T}][\mathbf{L}][\mathbf{C}]\mathbf{p}_{\text{MCMF}} \quad (1)$$

where  $[\mathbf{L}]$ ,  $[\mathbf{C}]$  are matrices of the lunar orientation;  $[\mathbf{T}]$  represents a matrix of the lunar position; and  $[\mathbf{B}]$ ,  $[\mathbf{P}]$ ,  $[\mathbf{N}]$ ,  $[\mathbf{II}]$ , and  $[\mathbf{\Theta}]$  are used to describe the earth irregular rotation.

After transforming the Moon-based platform's position into ITRS, some geometric parameters used in the entrance pupil radiation calculation can be calculated, including the nadir point, light ray vector  $\mathbf{l}$ , viewing angle, and angle  $\beta$  in Fig. 1.

Nadir is the intersection between the looking vector pointing to the earth's barycenter and the earth ellipsoid. In this study, the radiation emitted from the TOA of the earth was assumed to be at an altitude of 100 km [12]. Thus, the ellipsoid model was defined based on the earth ellipsoid

$$\frac{x^2 + y^2}{(a + 100)^2} + \frac{z^2}{(b + 100)^2} = 1 \quad (2)$$

where  $(x, y, z)$  are earth's coordinates at TOA in the ITRS, and  $a$  and  $b$  are the equatorial and polar radii of the earth ellipsoid.

The nadir point calculation is more complex when considering the model as an ellipsoid. The first step is to calculate the intersection point  $(x_{\text{geo}}, y_{\text{geo}}, z_{\text{geo}})$  described by Cartesian coordinates. Denoting the determined intersection as  $(x_{\text{geo}}, y_{\text{geo}}, z_{\text{geo}})$ , the Moon-based platform's position as  $(x_{\text{pos}}, y_{\text{pos}}, z_{\text{pos}})$ , and the looking vector as  $(x_{\text{los}}, y_{\text{los}}, z_{\text{los}})$ , the intersection points can be calculated by [31]

$$\begin{bmatrix} x_{\text{geo}} \\ y_{\text{geo}} \\ y_{\text{geo}} \end{bmatrix} = k \begin{bmatrix} x_{\text{los}} \\ y_{\text{los}} \\ y_{\text{los}} \end{bmatrix} + \begin{bmatrix} x_{\text{pos}} \\ y_{\text{pos}} \\ y_{\text{pos}} \end{bmatrix} \quad (3)$$

where  $k$  is a scale factor. Since the looking vector points to earth's barycenter, it can be numerically equivalent to the Moon-based platform's position.

Then, latitude  $\delta$  and longitude  $\eta$  can be expressed as

$$\delta = \arctan \left( \frac{z_{\text{geo}}/a}{\sqrt{x_{\text{geo}}^2 + y_{\text{geo}}^2 - w}} \right) \quad (4)$$

$$\eta = \arctan2 \left( \frac{y_{\text{geo}}/a}{x_{\text{geo}}} \right) \quad (5)$$

where  $w$  is determined through an iterative process

$$w_{\text{new}} = e^2(\rho - w_{\text{old}}) / \sqrt{(\rho - w_{\text{old}})^2 + (1 - e^2) \left( \frac{z_{\text{geo}}}{a} \right)^2} \quad (6)$$

where  $e$  is the eccentricity of the ellipsoid model.

The light ray is the base of the calculation of the viewing angle and the angle  $\beta$ . The vector  $|\vec{\mathbf{PT}}|$  is the light ray from the earth's position ( $\mathbf{t}_{\text{ITRS}}$ ) to the entrance pupil of the Moon-based active cavity radiometer. Light ray vector  $\mathbf{l}_{\text{ITRS}}$  can be expressed as

$$\mathbf{l}_{\text{ITRS}} = \mathbf{p}_{\text{ITRS}} - \mathbf{t}_{\text{ITRS}}. \quad (7)$$

The viewing angle is one of the most important parameters in ADM. To acquire the viewing angle of the position on the TOA of the earth, the core is to transform the light ray from ITRS to the local topocentric coordinate system (LT). The transform

process was as follows:

$$\mathbf{l}_{\text{LT}} = \begin{bmatrix} -\sin\eta' & \cos\eta' & 0 \\ -\sin\delta'\cos\eta' & -\sin\delta'\sin\eta' & \cos\delta' \\ \cos\delta'\cos\eta' & \cos\delta'\sin\eta' & \sin\delta' \end{bmatrix} \mathbf{l}_{\text{ITRS}} \quad (8)$$

where  $\delta'$  and  $\eta'$  are the latitude and longitude of this specific position.

Denoting the light ray's coordinates in the LT as  $(x_1, y_1, z_1)$ , the viewing angle including the azimuth and zenith angles can be derived from the transformed light ray

$$\begin{bmatrix} \varphi \\ \theta_v \\ D \end{bmatrix} = \begin{bmatrix} \tan^{-1} \frac{y_1}{x_1} \\ \frac{\pi}{2} - \tan^{-1} \frac{\sqrt{x_1^2 + y_1^2}}{z_1} \\ \sqrt{x_1^2 + y_1^2 + z_1^2} \end{bmatrix}. \quad (9)$$

Observing the EOR from a Moon-based platform has one main peculiarity—the long Earth–Moon distance. The observational scope of a Moon-based active cavity radiometer is almost half of the earth. This is a benefit for eliminate spatio-temporal sampling error. In this observation geometry, the EOR's calculation at the entrance pupil of the radiometer is essentially the integral of the radiation emitted from the observational scope. The Earth–Moon distance changes and the orbit of the Moon is approximately elliptical. The maximum distance is  $\sim 40\,000$  km, which significantly affects the observation geometry. Furthermore, the angle between the lunar and terrestrial equators is not fixed. The obliquity of the ecliptic and lunar declination determines the variation range of this angle.

### B. Analytical Method for OLR and OSR at the Entrance Pupil of the Moon-Based Active Cavity Radiometer

A Moon-based active cavity radiometer would measure the broadband OLR and OSR emitted and reflected from the earth. In such a special observation geometry, the observed EOR is the integral of the radiance over the portion of the earth in the observational scope. However, in contrast to the OLR, the calculation of OSR needs to make clear the earth's phase (i.e., the intersectional region between the observational scope and the sunlit part in Fig. 1), which can be expressed as the intersection angle between the Sun rays and looking vector

$$\varphi_s = \frac{\mathbf{l} \cdot \mathbf{s}}{|\mathbf{l}| |\mathbf{s}|} \quad (10)$$

where  $\mathbf{s}$  is the sunlit vector. Thus, the integration of OLR and OSR observed from all the points of TOA on earth within the observational scope is given by

$$F_M(\delta, \eta) = \int_{\Omega} I_{\text{TOA}}(\delta', \eta') X \cos\beta d\Omega \quad (11)$$

where  $(\delta, \eta)$  are nadir point positions of the Moon-based platform;  $(\delta', \eta')$  are the TOA point of the earth within the observational scope;  $\Omega$  is the solid angle subtended at the radiometer;  $\beta$  is the angle between the nadir and the line of the radiometer to location  $(\delta', \eta')$ ; and  $X$  is the unified expression of the ADM. For the OLR,  $X$  is the  $X_{\text{OLR}}(\theta_v)$ , which is the longwave ADM as a function of the viewing zenith angle  $\theta_v$ ; and  $X_{\text{OSR}}(\theta_s, \theta_v, \varphi)$

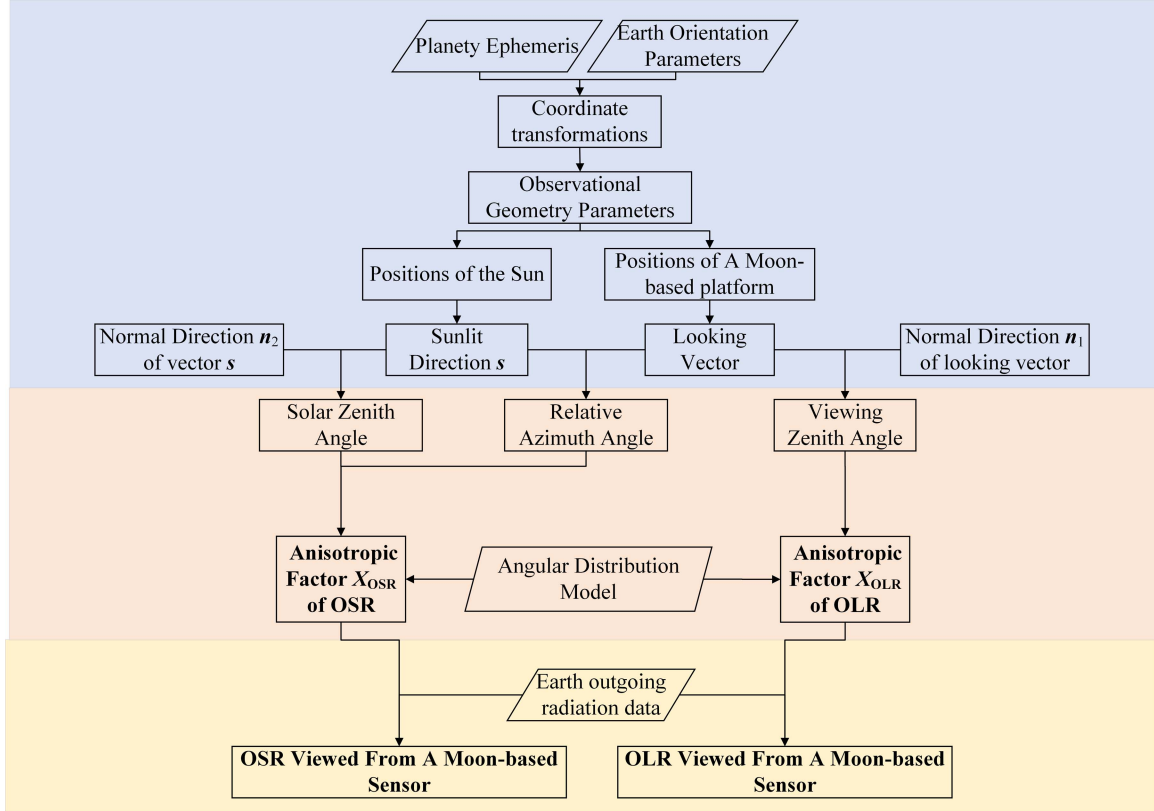


Fig. 2. Scheme of the proposed method.

is the shortwave ADM as a function of solar zenith angle  $\theta_s$  and viewing zenith angle  $\theta_v$ .

Integrating all angles over the hemisphere defined by the zenith and azimuth angles, we get the normalization condition

$$2 \int_0^{\frac{\pi}{2}} X \sin\theta_v \cos\theta_v d\theta_v = 1. \quad (12)$$

Since the radiometer observes the EOR only for a given direction, the flux emitted from the TOA is anisotropic, and certain epirical adjustments are required. The ADM  $X$  is used to display the anisotropic characteristics (OLR or OSR), which can be written in the form

$$X = \frac{F_{\text{TOA}}(\delta', \eta')}{\pi I_{\text{TOA}}(\delta', \eta')}. \quad (13)$$

The function is determined based on the radiative transfer theory as well as observations for specific positions.

We express the  $I_{\text{TOA}}(\delta', \eta')$  at a point on the TOA of the earth as

$$I_{\text{TOA}}(\delta', \eta') = \frac{F_{\text{TOA}}(\delta', \eta') X}{\pi} \quad (14)$$

where  $F_{\text{TOA}}(\delta', \eta')$  is the flux of this point in  $\text{W m}^{-2}$ .

Thus, (11) can be rewritten to give the measurement in terms of the flux at TOA

$$F_M(\delta, \eta) = \int_{\Omega} \frac{F_{\text{TOA}}(\delta', \eta') X}{\pi} \cos\beta d\Omega. \quad (15)$$

Given the total EOR at TOA ( $F_{\text{TOA}}$ ) for all points in the observational scope, the radiances at the entrance pupil of the radiometer can be calculated. For the OSR, the flux at TOA depends on incoming shortwave radiance  $F_{\text{solar}}$  and the albedo of the earth  $\alpha$ . Thus, (15) can also be expressed as

$$F_M(\delta, \eta) = \int_{\Omega} \frac{F_{\text{solar}} \alpha(\delta', \eta') X}{\pi} \cos\beta d\Omega. \quad (16)$$

### III. EXPERIMENT AND DISCUSSION

Next, we conducted experiments to test the processing of OLR data.

#### A. Data Description

NASA's Goddard Earth Observing System Model, Version 5 (GEOS-5) is an integrated system of models to support global climate studies, including the atmospheric general circulation model (AGCM) and analysis of observational sources of information [32], [33]. The GEOS-5 model can provide global, seasonal-to-decadal climate simulations of the EOR. In the GEOS-5 model simulation, the EOR is held to within approximately  $1 \text{ W m}^{-2}$ , which is close to estimates of the real case. For OLR and OSR, the general distribution of GEOS-5 AGCM OLR and OSR matched well with that of CERES Energy Balanced and Filled (EBAF).

In this model, 1152 longitudinal and 721 latitudinal grid points, with a spatial resolution of approximately  $34 \times 27 \text{ km}$

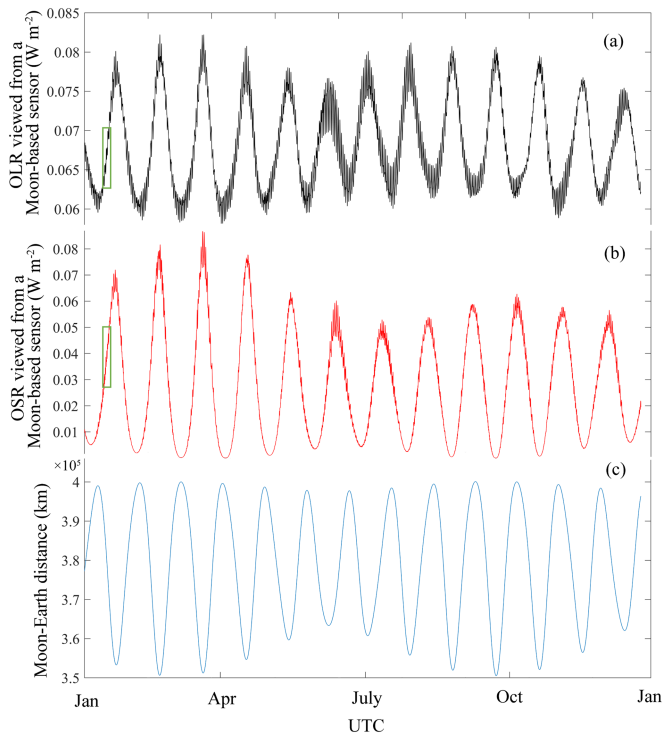


Fig. 3. Variation in (a) outgoing longwave radiation (OLR) viewed from a Moon-based sensor, (b) outgoing shortwave radiation (OSR) viewed from a Moon-based sensor, and (c) the Moon–Earth distance during 2015. The green box marks the period shown in detail in Fig. 4.

along the earth’s equator are produced. In simulations of EOR, global fluxes are produced every hour. Arbitrarily, we chose a 1-year output from 1 January 2015 to simulate Moon-based active capacity measurements.

For calculation of the Moon’s orbit and lunar libration, the Jet Propulsion Laboratory (JPL) Development Ephemeris (DE) was adopted [34]. DE tabulates geocentric coordinates and libration of the Moon. The positions are recorded as a  $(t; x, y, z)$  coordination, which is in the coordinate system of the International Celestial Reference System (ICRS) and time system of Dynamical Barycentric Time (TDB). The lunar libration angles are recorded as a  $(t; \phi_m, \theta_m, \psi_m)$ , which is used as the lunar orientation information. Since the earth’s rotation is not constant over time, EOPs are used to describe the irregular rotation of the earth. The EOPs provide the rotational transform from the ICRS to ITRS, as a function of time.

### B. Results

The scheme used for the estimation of the Moon-based earth observation geometric parameters and simulation of the EOR measurements is shown in Fig. 2. The processing steps were designed to create the Moon-based earth observation geometry and to simulate measurements of OLR and OSR as realistically as possible.

In the preprocessing phase, the Moon-based earth observation geometry was parameterized according to the model introduced in Section II. Essentially, the observation geometry refers to the geometric relationship between the Moon-based platform’s

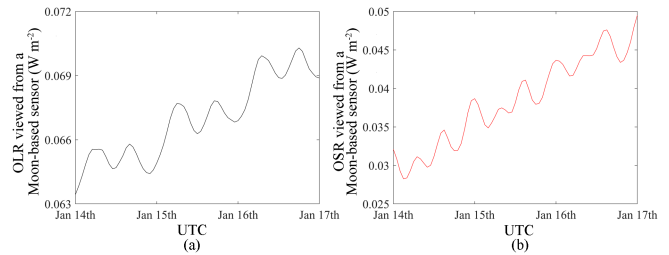


Fig. 4. Variation in (a) outgoing longwave radiation (OLR) and (b) outgoing shortwave radiation (OSR) from January 14 to January 16, 2015.

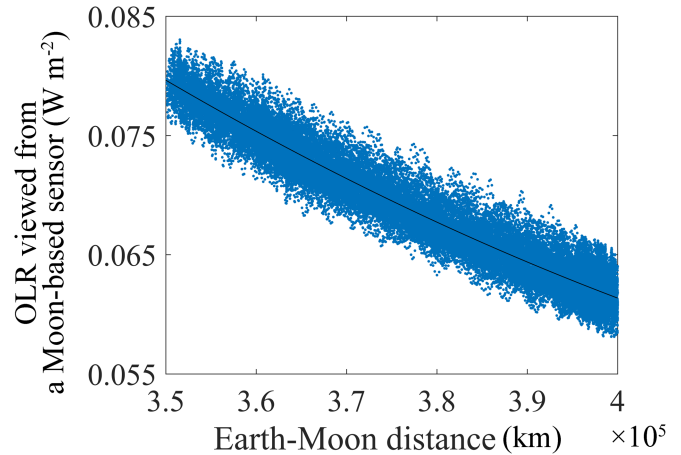


Fig. 5. Relationship between the Earth–Moon distance and outgoing longwave radiation (OLR) viewed from a Moon-based sensor. The black line is the polynomial curve; the equation of the line quadratic and its coefficient is greater than zero.

position and points on earth. Two main parameters, the Moon-based platform’s position and observational scope were calculated. From (3), if the point on earth is in the observational scope, there are two solutions for  $\lambda$ . If the solutions shrink into one, the light ray is tangent to the ellipsoid. The observational scope can be seen as the link line of the tangent points between the light ray and ellipsoid. Since the GEOS-5 model data is in the form of  $0.3125^\circ$  longitude  $\times$   $0.25^\circ$  latitude, the observational scope is then discretized in a corresponding size. The Moon-based platform’s position was used to calculate the looking vector and the light ray, which are important factors for calculating the OLR of one element. The angle between the light ray and normal vector of the element observation point is the viewing zenith angle, and is an output of determining the anisotropic of element. The other outputs were the cloud properties and scene type. In the ADM, cloud properties mainly refer to cloud coverage; according to the ratio of cloud cover to sky areas, every element can be divided into clear sky (5% or less), partly cloudy (5%–50%), mostly cloudy (50%–95%), and overcast (95% or more). Meanwhile, the scene type can also be split into four categories: ocean, land, snow, and desert. If an element is a mixed, its type depends on which surface feature has the largest proportion. The anisotropic factor of each element was also derived. Integrating the OLR of each element until all the

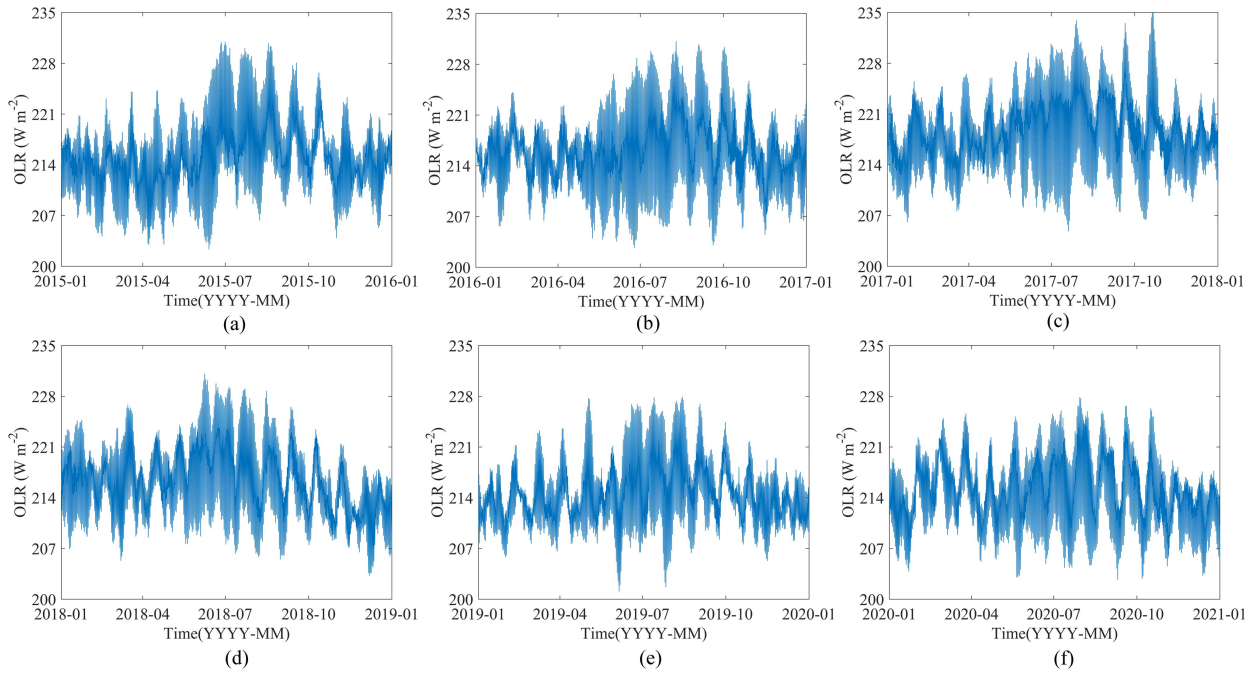


Fig. 6. Outgoing longwave radiation (OLR) variation after removing the effect of Moon–Earth distance in (a) 2015, (b) 2016, (c) 2017, (d) 2018, (e) 2019, and (f) 2020.

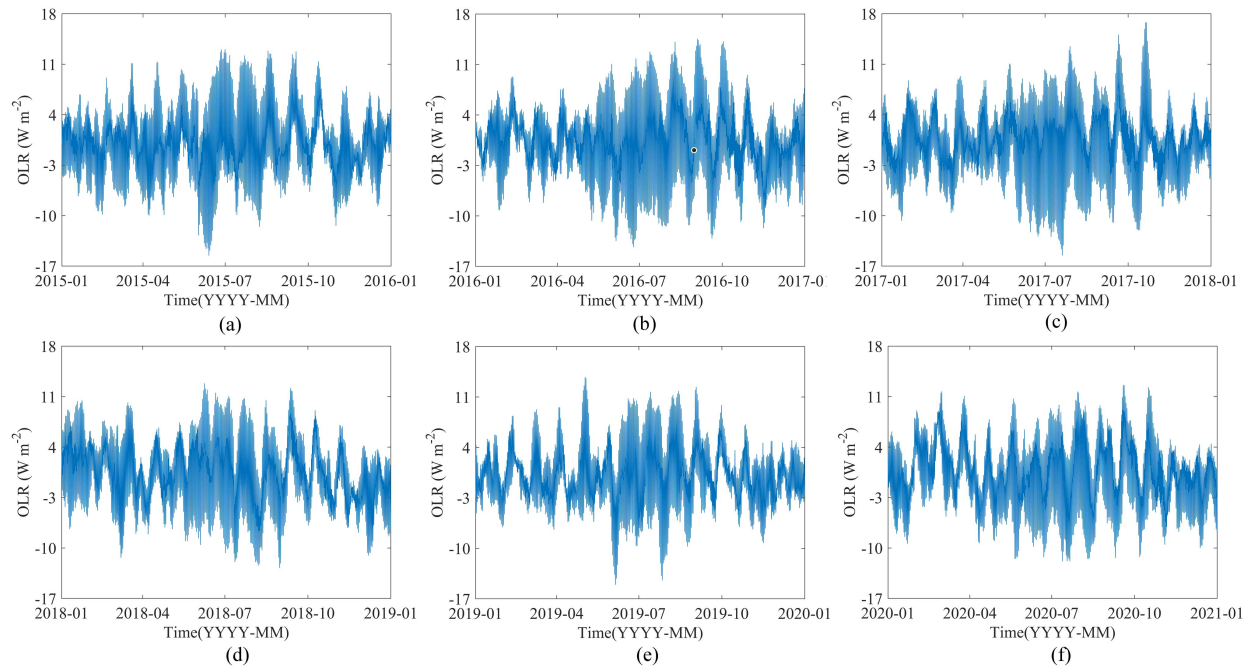


Fig. 7. Outgoing longwave radiation (OLR) variation after removing the effect of seasonal variation in (a) 2015, (b) 2016, (c) 2017, (d) 2018, (e) 2019, and (f) 2020.

elements were considered, the total OLR in the observation scope was finally calculated.

Fig. 3(a) and (b) shows OLR and OSR variations viewed from a Moon-based sensor from January 1 to December 31, 2015, respectively, assuming a Moon-based sensor located at the center of the lunar disk. It is clear that both OLR and OSR

have a period corresponding to the orbital cycle of  $\sim 27.3$  days. The maximum OLR value was  $82 \text{ mW m}^{-2}$  and occurred in March, when the Sun moves near the equator. The minimum OLR ( $\sim 58 \text{ mW m}^{-2}$ ) also appeared in March, delayed one half period from the maximum value. The difference between the maximum and minimum ( $24 \text{ mW m}^{-2}$ ) accounted for  $\sim 30\%$  of

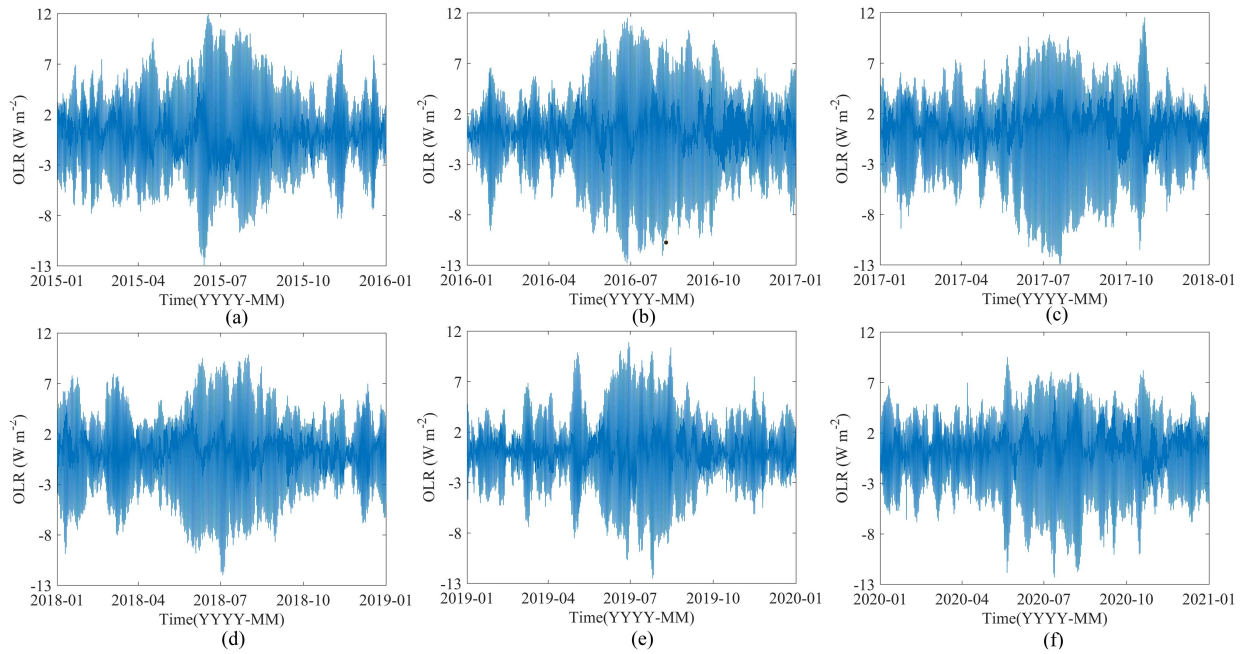


Fig. 8. Outgoing longwave radiation (OLR) variation after removing the effects of diurnal variation in (a) 2015, (b) 2016, (c) 2017, (d) 2018, (e) 2019, and (f) 2020.

the average OLR in 2015. The maximum and minimum values in each orbital period also had periods of  $\sim 0.5$  years, with peaks in March and September (and the minimum in June). The maximum and minimum OSR coincided with those of OLR. However, when the minimum OSR was reached ( $0.004 \text{ mW m}^{-2}$ ), the earth sunlit part could barely be seen by a Moon-based sensor. Both OLR and OSR viewed from a Moon-based sensor and the Moon–Earth distance have the same variation period; however, the maximum values of EOR were coincident with the minimum distance. Thus, distance plays a significant role in the measurement of EOR. Besides, the observed OLR depended on the earth’s scene; thus, there were small oscillations in every period, which were especially obvious in each peak and valley.

For a more detailed analysis, we focused on EOR from January 14 to January 16, 2015, and found that it did not change continuously (see Fig. 4). There were distinct daily cycles in which the OLR had two peaks and two valleys, probably because of differences in the earth scene. Peaks corresponded to a Moon-based sensor field of view dominated by land, while valleys corresponded to a field of view dominated by ocean. After a daily cycle, the overall trend of OLR increased because the Moon and earth moved closer together during that time. From Fig. 3(a), we also found that the maximum oscillation occurred in June (almost  $6.4 \text{ mW m}^{-2}$ ), and the minimum oscillation was only  $1.4 \text{ mW m}^{-2}$ . The difference between the maximum and minimum oscillation (up to  $5 \text{ mW m}^{-2}$ ) is much smaller than the effect of Moon–Earth distance; however, it cannot be ignored. In contrast to OLR, OSR had more small oscillations owing to the joint influence of earth’s phase and scene.

In summary, thanks to changing inclination of lunar orbit, a Moon-based platform can observe the earth in different directions with continuous angles. OLR and OSR were not only

affected by the Moon–Earth distance but were influenced by earth’s phase, for OLR is earth’s scene and for OSR is observational scope. These effects should not be neglected.

### C. Discussion

1) *Effects of Moon–Earth Distance to OLR*: Fig. 5 shows the relationship between the Moon–Earth distance and OLR viewed from the Moon-based sensor from 2015 to 2020. The minimum OLR reached  $58 \text{ mW m}^{-2}$  and the maximum was  $83 \text{ mW m}^{-2}$ . The difference between them accounts for nearly 40% of the average OLR in 2015. Meanwhile, the Moon–Earth distance varied from  $3.5 \times 10^5$  to  $4 \times 10^5$  km. With increasing distance, the OLR significantly decreased. The data have a polynomial curve, for which the equation is quadratic, and the coefficient is greater than zero which is shown as  $y = 1.566 \times 10^{-12}x^2 - 1.54x + 0.4286$ . Moreover, they can also be fitted with the radiation transmission equation.

Fig. 6 shows the OLR variation without the effects of the Moon–Earth distance from 2015 to 2020. OLR in these six years varied from 200 to  $235 \text{ W m}^{-2}$ . Six-year variations are used to show interannual variations of EOR, helping to figure out their similarities and differences. The annual differences between the maximum and minimum differed; the largest annual difference was in 2017 ( $\sim 31 \text{ W m}^{-2}$ ) and smallest was in 2020 ( $\sim 25 \text{ W m}^{-2}$ ). In all years, large oscillations occurred in the middle of the year, while small oscillations happened at the beginning and end of the year. OLR almost always reached both the maximum and minimum values in the summer, and the curves had normal distributions centered in the middle of one year. Root-mean-square error (rmse) is a potent indicator to reveal the intensity of OLR variation. Over the six years,

TABLE I  
CORRELATION COEFFICIENTS IN SIX YEARS OF OLR

Year	2015	2016	2017	2018	2019	2020
correlation coefficient 1 <sup>1</sup>	0.8197	0.8764	0.8517	0.8314	0.8569	0.8714
correlation coefficient 2 <sup>2</sup>	0.7502	0.7612	0.7552	0.6951	0.7106	0.6717

<sup>1</sup>correlation coefficient 1 represents correlation coefficient before and after removing OLR seasonal variations

<sup>2</sup>correlation coefficient 2 represents correlation coefficient before and after removing OLR diurnal variations

the rmse ranged from 16 to 21, with the minimum change in 2019. Compared with Fig. 3, OLR was characterised by more unordered and smaller variation, perhaps because the effect of cloud coverage was magnified. After removing the effects of Earth–Moon distance, the 27.3-day orbital cycle was not as distinct as in Fig. 3, but 13 peaks still existed.

In summary, removing the effects of Earth–Moon distance impacted on the OLR distribution and caused more frequent oscillations in summer. From the Moon moves from perigee to apogee, the OLR decreases almost 40% and OSR decreases about 60%.

2) *Seasonal and Diurnal Variations of OLR in the Earth's Moon-Facing Hemisphere:* OLR is also affect by seasonal variation. We assigned seasons according to the ERBE ADMs. By calculating the mean OLR of each season, we found that the maximum occurred in the summer, and most minima occurred in the winter. Over the six years, OLR in the summer changed significantly, but was more stable in the winter. The summer rmse were two to three times those of the winter. Fig. 7 shows OLR variation after removing the effects of seasonal variation from 2015 to 2020. Negative values represent OLR that is smaller than the seasonal average OLR. The absolute maximum and minimum values in each year were almost the same; the difference between them first increased and then decreased, and was largest in 2017. Compared with Fig. 6, for the entire year, rmse was lower (15–19). OLR varied more smoothly and the 27.3-day cycle was less and less obvious.

Although OLR variations over six years showed significant differences, the maximum and minimum values no longer occurred only in summer; that is, the curves of OLR became smoother.

Fig. 8 shows OLR variation after removing the effect of diurnal variation. OLR variation was obviously smoothed, and the rmse within each year was just 9–14. However, the number of oscillations increased. With 0 as the dividing limit, fluctuations of the upper and lower parts of the curve were almost the same, and the average of OLR was only on the magnitude of  $10^{-17}$ . OLR changed dramatically in the middle of each year; the curves in Fig. 8 are dense in the middle and scattered on both sides. The range of OLR was smaller and the maximum and minimum values converged over six years. In summary, after removing the effect of diurnal variation, the orbital cycle almost disappeared.

Table I is two correlation coefficients in six years. The first line represents correlation coefficient before and after removing OLR seasonal variations and the second line represents correlation coefficient before and after removing OLR diurnal variations. It's obvious that mean value of coefficient 1 is bigger than coefficient 2, meaning the diurnal variations have greater influence than seasonal variations, and hemisphere-scale

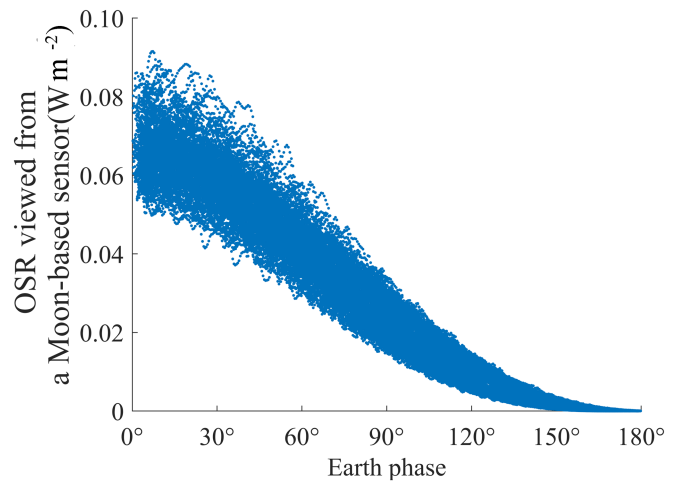


Fig. 9. Relationship between earth phase and outgoing shortwave radiation (OSR) viewed from a Moon-based sensor.

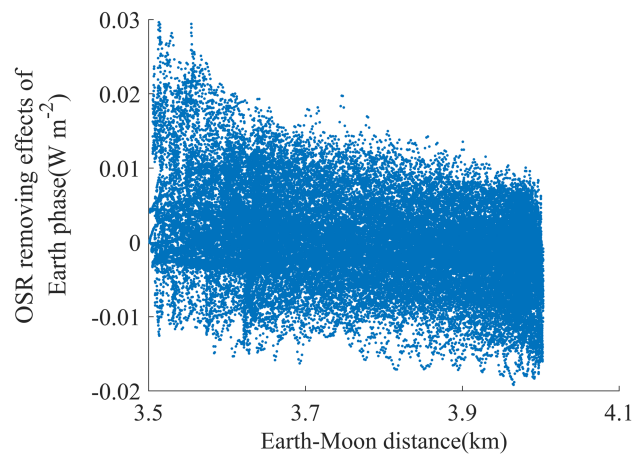


Fig. 10. Relationship between earth phase and outgoing shortwave radiation (OSR) removing the effects of Earth–Moon distance viewed from a Moon-based sensor.

observations smooth out the effects of seasons. For different years, both two coefficients reach to maximum in 2016 and coefficient 1 reaches to minimum in 2015 and coefficient 2 is 2020, thus, OLR also represents interannual difference.

In summary, our results show that with increasing distance, OLR significantly decreases and can be written in a negative quadratic form. After removing the effects of Earth–Moon distance, the OLR is within the Moon-based platform's observational scope, and the magnitude changes from  $10^{-2}$  to  $10^3$ . Meanwhile, the orbital cycle becomes less distinct and seasonal variation is protruded. After removing seasonal and



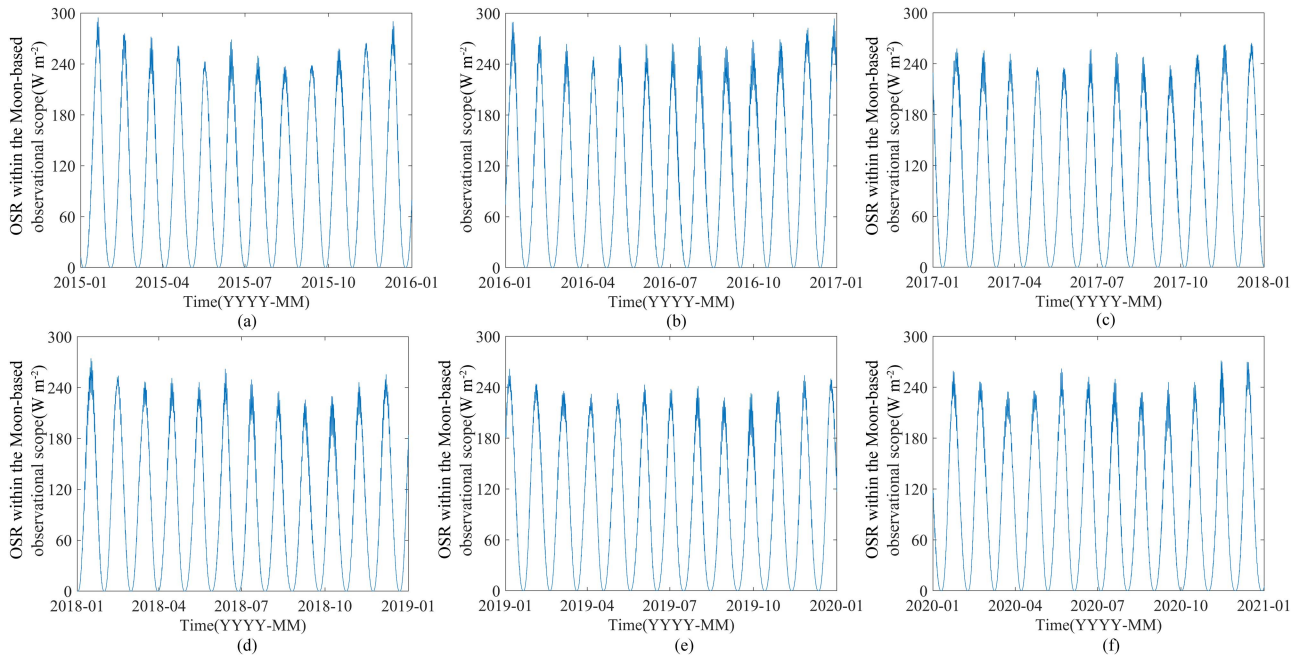


Fig. 11. Variation of outgoing shortwave radiation (OSR) within the Moon-based observational scope in (a) 2015, (b) 2016, (c) 2017, (d) 2018, (e) 2019, and (f) 2020.

diurnal variations, the line curve of OLR is smoother with fewer oscillations. Compared correlation coefficients, the diurnal variations have greater influence than seasonal variations for six years. Thus, Earth–Moon distance, seasonal changes, and earth rotation all affect OLR viewed from a Moon-based sensor, and hemisphere-scale observations may smooth out the effects of seasons.

3) *Effects of Earth's Phase on OSR*: The scope of OSR is subject to the sunlit region. Thus, the variation of OSR viewed from a Moon-based sensor was much larger than that of OLR. A Moon-based platform can observe the earth in different phases. When the earth's phase is equal to  $0^\circ$ , the sunlit vector and looking vector are in the same direction. At this moment, a Moon-based sensor can observe almost a whole hemisphere of the sunlit earth as the OLR scene. Moreover, a solar eclipse occurs at this time. At this point, the OSR reached its maximum ( $\sim 0.092 \text{ W m}^{-2}$ ). In contrast, when the earth's phase is equal to  $180^\circ$ , the Sun, earth, and Moon are on a same line with the earth in the middle. At this moment, the earth is sunless and an eclipse of the Moon occurs. At this point, the OSR reached its minimum ( $\sim 5.5 \times 10^{-13} \text{ W m}^{-2}$ ). The difference of earth's phase over the next 2 days was from  $4.2 \times 10^{-4}^\circ$  to  $0.6^\circ$ , mostly concentrated between  $0.4^\circ$  and  $0.6^\circ$ . Meanwhile, the difference in OSR varied from  $2.7 \times 10^{-14}$  to  $4 \times 10^{-3} \text{ W m}^{-2}$ . While the differences in the earth's phase and OSR did not have a distinct linear correlation, we still found that when the difference in the earth's phase was less than 0.3, the variation of OSR was not more than  $2 \times 10^{-4} \text{ W m}^{-2}$ . In contrast, if the difference in the earth's phase was more than 0.3, the change in OSR could reach  $4 \times 10^{-3} \text{ W m}^{-2}$ . Thus, OSR viewed from a Moon-based sensor is inversely proportional to the earth's phase, as shown in Fig. 9. However, earth's phase is not treated as influence factor

to OSR, it is more like attribute for OSR. Then, what are other factors that can influence OSR? Fig. 10 is the relationship between Earth–Moon distance and OSR after removing the effects of earth's phase. It is clear that OSR also has a negative quadratic relationship with the Earth–Moon distance. From the Moon from perigee to apogee, the OSR can decrease by 60%.

According to (16), the OSR viewed from a Moon-based sensor is not only related to the observation solid angle (which depends on the earth's phase), but also to incoming solar radiation. Fig. 11 shows OSR variation within the Moon-based observational scope from 2015 to 2020. That is, OSR after removing the effects of observation solid angle. In different years, OSR within the Moon-based observational scope had the same trend. The minimum was when the earth's phase was  $180^\circ$  and the maximum was when the earth's phase was  $0^\circ$ . There was a distinct cycle corresponding to the lunar orbit. In one year, OSR first decreased and then increased, reaching the maximum in June or July. It then decreased to a minimum in November or December. Although the OSR variations among the six years were similar, the maximum values ranged from 261 to  $294 \text{ W m}^{-2}$ .

Fig. 12 shows the variation in ISR of TOA from 2015 to 2020. For every year, the ISR trend was almost the same, varying from 0 to  $950 \text{ W m}^{-2}$  and explicating an approximately monthly cycle. Each cycle has its maximum and minimum. For the maximum values, the larger one occurred in the winter when the subsolar point was to the south of the earth, and the smaller one occurred in the summer. As for the minimum values, the smaller one also occurred in the summer, however, the bigger one contributed in the spring and autumn in responses to the Sun–Earth distance and the earth's phase.

Fig. 13 shows the ratio between the OSR of the Moon-based observational scope and the ISR (OSR/ISR) over the six years.

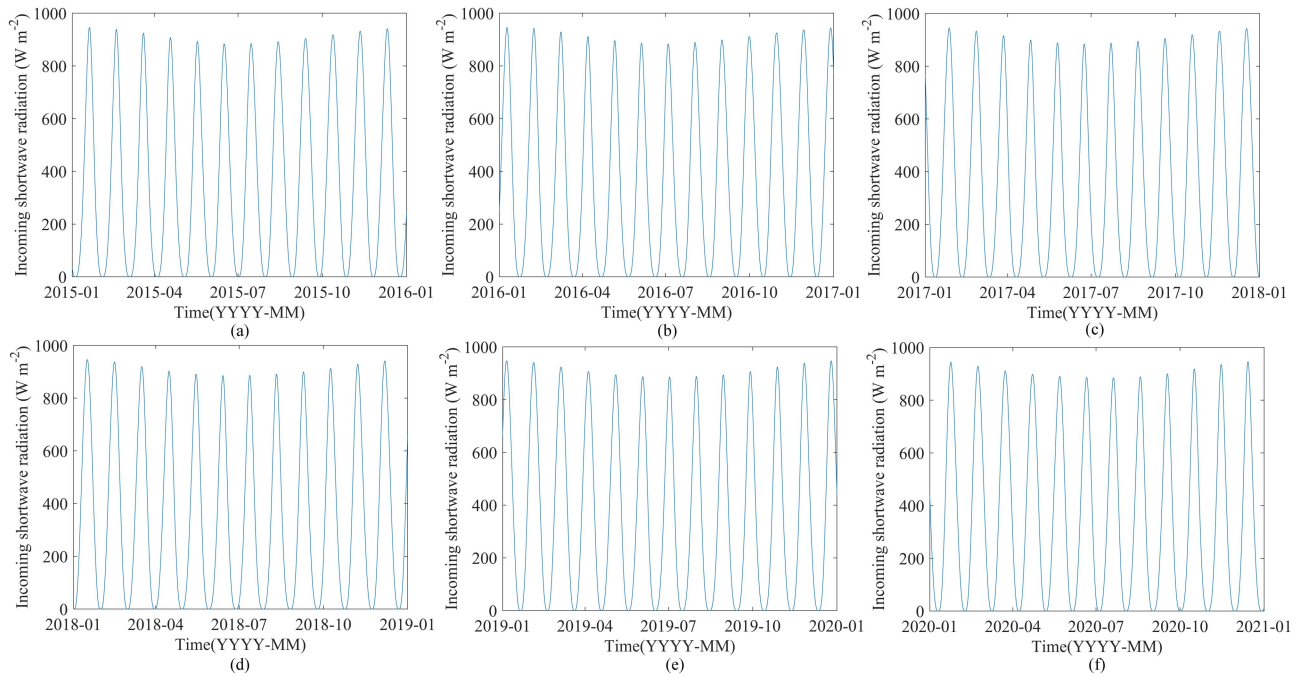


Fig. 12. Top-of-atmosphere (TOA) incoming shortwave radiation variation in (a) 2015, (b) 2016, (c) 2017, (d) 2018, (e) 2019, and (f) 2020.

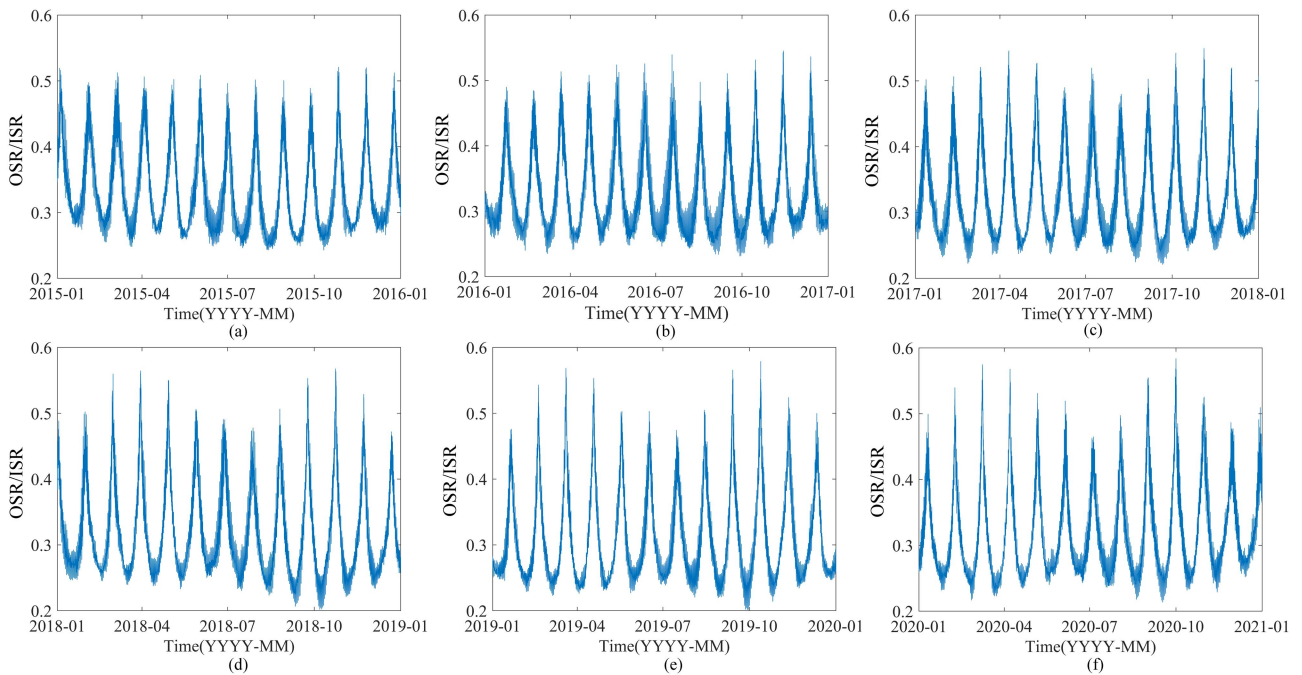


Fig. 13. Outgoing shortwave radiation (OSR)/incoming shortwave radiation (ISR) within a Moon-based platform observational scope in (a) 2015, (b) 2016, (c) 2017, (d) 2018, (e) 2019, and (f) 2020.

This ratio records the absorbed or reflected ability of the earth’s surface to ISR, varied from 0.25 to 0.58. OSR/ISR is not same as earth’s surface albedo or TOA albedo. It is used to remove the effects of ISR to show OSR characteristics because both of them are affected by earth’s phase. It can also be interpreted as somewhat weakened effects of earth’s phase. The minimum

occurred when the earth’s phase was 0°, at which point the earth was fully sunlit within the observational scope. At this moment, almost all the earth scene was included, and the OSR/ISR was closest to the true earth albedo. Moreover, at this time, small changes in the earth’s phase resulted in small oscillations in OSR/ISR. In contrast, when the earth was far from fully sunlit,

the OSR/ISR ratio suddenly increased and then decreased to a normal value mainly owing to scene changes.

In our work, we mainly summarized three Moon-based earth EOR characteristics. Previous studies for Moon-based EOR observations can be divided into three directions. The first is for EOR monitoring from aspect of Moon-based earth observation geometry. Ye investigated the temporal sampling error on the EOR and found the suitable sampling time for EOR [35]. Duan calculated the EOR earth observational coverage ratio for a Moon-based platform [36]. The second is radiation simulation including anisotropy characteristics analysis from sun a long distance. Wu and Shang [37], [38] described the anisotropy and isotropy difference, and found anisotropic surface reflection need to be considered by Moon-based earth observations. The third is radiation quantification, trying to monitoring EOR more precisely. Ye [39] explored the ellipsoidal earth model rather than spherical model for EOR monitoring. Duan [40] precisely divided the observational scope to  $2048 \times 2048$  pixels to improve EOR monitoring. Our work is the extension of previous work and have significant role in EOR monitoring.

#### IV. CONCLUSION

Based on the observation geometry of a Moon-based platform and an outgoing radiation calculation method at the entrance pupil of the Moon-based radiometer, this article mainly answers the question that what characteristics for Moon-based EOR observations, and what are its peculiarities compared to existing satellites. The simulated measured OLR and OSR have the same period as the Earth–Moon distance and correspond to the orbital cycle. With increasing distance, OLR and OSR significantly decreased by about 40% and 60%. Their relationships can be written in a negative quadratic form. After removing the effect of Earth–Moon distance, OLR has a seasonal distribution, with large oscillations often occurring in the summer and small oscillations occurring in the winter. This is partly owing to the changing ratio of scene type and cloud coverage. Moreover, the line curve of OLR is smoother after removing the effects of seasonal and diurnal variations. Compared correlation coefficients before and after removing seasonal and diurnal variations, the latter have greater influence than the former, meaning hemisphere-scale observations is less sensitive to seasonal signals. OSR is inversely proportional to earth's phase. Using the ratio between OSR and ISR can remove the effects of earth's phase, and its value is close to earth albedo when the earth's phase is  $0^\circ$ . With the development of international lunar research stations, Moon-based earth observations as one of its scientific goals can be a new area of study. The results of this study will help to facilitate Moon-based monitoring of EOR.

#### ACKNOWLEDGMENT

GOES-5 data were obtained from the NASA Goddard Earth Observing System Model, Version 5 (GOES-5) and are available from the Goddard Global Modeling and Assimilation Office<sup>1</sup>.

<sup>1</sup>[http://gmao.gsfc.nasa.gov/global\\_mesoscale/](http://gmao.gsfc.nasa.gov/global_mesoscale/)

#### REFERENCES

- [1] H. Guo, G. Liu, and Y. Ding, "Moon-based Earth observation: Scientific concept and potential applications," *Int. J. Digit. Earth*, vol. 11, no. 6, pp. 546–557, 2018.
- [2] S. Cornell, I. C. Prentice, J. House, and C. Downy, *Understanding the Earth System: Global Change Science for Application*. Cambridge, U.K.: Cambridge Univ. Press, 2012.
- [3] J. H. Lawton, "Earth system science," *Science*, vol. 292, no. 5524, pp. 1965–1965, 2001.
- [4] N. G. Loeb et al., "Observed changes in top-of-the-atmosphere radiation and upper-ocean heating consistent within uncertainty," *Nat. Geosci.*, vol. 5, no. 2, pp. 110–113, Feb. 2012.
- [5] J. T. Suttles et al., "Angular radiation models for earth-atmosphere system. Volume 2: Longwave radiation," *NASA Reference Pub.*, Washington, DC, USA, 1989.
- [6] J. T. Suttles et al., "Angular radiation models for earth-atmosphere system. Volume 1: Shortwave radiation," *NASA Reference Pub.*, vol. 1184, p. 147, 1988.
- [7] D. L. Hartmann, V. Ramanathan, A. Berroir, and G. E. Hunt, "Earth radiation budget data and climate research," *Rev. Geophys.*, vol. 24, no. 2, pp. 439–468, 1986.
- [8] I. M. Vardavas and K. Koutoulaki, "A model for the solar radiation budget of the northern hemisphere: Comparison with Earth radiation budget experiment data," *J. Geophys. Res. Atmos.*, vol. 104, no. D8, pp. 9489–9500, 1999.
- [9] B. A. Wielicki, B. R. Barkstrom, E. F. Harrison, R. B. L. Iii, G. L. Smith, and J. E. Cooper, "Clouds and the Earth's radiant energy system (CERES): An earth observing system experiment," *Bull. Amer. Meteorol. Soc.*, vol. 36, no. 4, pp. 1127–1141, 1998.
- [10] H. Jacobowitz, H. V. Soule, H. L. Kyle, and F. B. House, "The earth radiation budget (Erb) experiment - an Overview," *J. Geophys. Res. Atmos.*, vol. 89, no. Nd4, pp. 5021–5038, 1984.
- [11] F. B. House, A. Gruber, G. E. Hunt, and A. T. Mecherikunnel, "History of satellite missions and measurements of the Earth radiation budget (1957–1984)," *Rev. Geophys.*, vol. 24, no. 2, pp. 357–377, 1986.
- [12] N. G. Loeb et al., "Angular distribution models for top-of-Atmosphere radiative flux estimation from the clouds and the Earth's radiant energy system instrument on the tropical rainfall measuring mission satellite. Part I: Methodology," *J. Appl. Meteorol.*, vol. 42, no. 4, pp. 240–265, 2003.
- [13] A. K. Shrestha et al., "Spectral unfiltering of ERBE WFOV nonscanner shortwave observations and revisiting its radiation dataset from 1985 to 1998," in *Proc. Int. Radiat. Symp.*, 2017, pp. 379–390.
- [14] V. A. Golovko, *The Earth Radiation Budget, 20 Years Later (1985–2005)*. Heidelberg, Germany: Springer, 2009, pp. 37–61.
- [15] N. G. Loeb et al., "Clouds and the Earth's radiant energy system (CERES) energy balanced and filled (EBAF) top-of-atmosphere (TOA) edition-4.0 data product," *J. Climatol.*, vol. 31, no. 2, pp. 895–918, 2018.
- [16] P. Minnis, D. F. Young, S. Sunmack, D. R. Doelling, and Q. Z. Trepte, "CERES cloud property retrievals from imagers on TRMM, Terra, and Aqua," in *Proc. Remote Sens. Clouds Atmos. VIII*, 2004, pp. 37–48.
- [17] G. Matthews, "In-flight spectral characterization and calibration stability estimates for the clouds and the earth's radiant energy system (CERES)," *J. Atmos. Ocean. Technol.*, vol. 26, no. 9, pp. 1685–1716, 2008.
- [18] M. Folkman, P. Jarecke, T. Hedman, and S. Carman, "Calibration of a shortwave reference standard by transfer from a blackbody standard using a cryogenic active cavity radiometer," in *Proc. Geosci. Remote Sens. Symp., Surf. Atmos. Remote Sens.: Technol., Data Anal. Interpretation, Int.*, vol. 4, 1994, pp. 2298–2300.
- [19] S. Kato, N. G. Loeb, D. A. Rutan, and F. G. Rose, "Clouds and the Earth's radiant energy system (CERES) data products for climate research," *J. Meteorol. Soc. Jpn.*, vol. 93, no. 6, pp. 597–612, 2015.
- [20] J. E. Harries et al., "The geostationary Earth radiation budget project," *Bull. Amer. Meteorol. Soc.*, vol. 86, no. 7, pp. 945–960, 2005.
- [21] H. Qiu, L. Hu, Y. Zhang, D. Lu, and J. Qi, "Absolute radiometric calibration of Earth radiation measurement on FY-3B and its comparison with CERES/Aqua data," *IEEE Trans. Geosci. Remote Sens.*, vol. 50, no. 12, pp. 4965–4974, 2012.
- [22] J. Burt and B. Smith, "Deep space climate observatory: The DSCOVR mission," in *Proc. IEEE Aerosp. Conf.*, 2012, pp. 1–13.
- [23] F. P. J. Valero, "Keeping the DSCOVR mission alive," *Science*, vol. 311, no. 5762, pp. 775–776, Feb. 2006.
- [24] S. R. Lorentz, J. S. Briscoe, and A. W. Smith, "NISTAR: Continuous total and short wave measurements of the full sunlit Earth disk from L1," in *Proc. AGU Fall Meeting*, 2016, pp. A21K–A201.

- [25] B. A. Wielicki et al., "Achieving climate change absolute accuracy in orbit," *Bull. Amer. Meteorol. Soc.*, vol. 94, no. 10, pp. 1519–1539, 2013.
- [26] J. J. Grinstead, J. C. Chiu, R. J. Gurney, S. C. Han, and C. J. Morcrette, "Determination of global Earth outgoing radiation at high temporal resolution using a theoretical constellation of satellites," *J. Geophys. Res. Atmos.*, vol. 122, no. 2, pp. 1114–1131, 2017.
- [27] W. H. Swartz et al., "The RAVAN CubeSat mission: Advancing technologies for climate observation," in *Proc. Geosci. Remote Sens. Symp.*, 2015, pp. 5300–5303.
- [28] Y. T. Song, X. Q. Wang, S. S. Bi, J. T. Wu, and S. P. Huang, "Effects of solar radiation, terrestrial radiation and lunar interior heat flow on surface temperature at the nearside of the Moon: Based on numerical calculation and data analysis," *Adv. Space Res.*, vol. 60, no. 5, pp. 938–947, Sep. 2017.
- [29] Y. Z. Jia and Y. L. Zou, "Research on lunar site selection for lunar based Earth observation," *Spacecraft Eng.*, vol. 25, no. 6, pp. 116–121, 2016.
- [30] H. Ye, H. Guo, and G. Liu, "The coverage analysis for Moon-based platform at three- polar regions on Earth," in *Proc. IOP Conf. Ser.: Earth Environ. Sci.*, 2016, Art. no. 012024.
- [31] H. Ye, H. Guo, G. Liu, Q. Guo, and J. Huang, "Looking vector direction analysis for the Moon-based Earth observation optical sensor," *IEEE J. Sel. Topic Appl. Earth Observ. Remote Sens.*, vol. 11, no. 11, pp. 4488–4499, Nov. 2018.
- [32] L. T. Andrea Molod, M. Suarez, J. Bacmeister, I.-S. Song, and A. Eichmann, "The GEOS-5 atmospheric general circulation model: Mean climate and development from MERRA to fortuna," *Tech. Rep. NASA*, Tech. Rep. NASA/TM-2012-104606, 2012.
- [33] M. M. Rienecker et al., "The GEOS-5 data assimilation system - documentation of versions 5.0.1, 5.1.0, and 5.2.0," *Tech. Memo. NASA*, Tech. Rep. NASA/TM-2008-104606-VOL-27, 2008.
- [34] E. M. Standish, "The JPL planetary and lunar ephemerides DE402/LE402," *Bull. Amer. Astron. Soc.*, vol. 27, 1995, Art. no. 1203.
- [35] H. Ye, H. Guo, G. Liu, J. Ping, L. Zhang, and Y. Zhang, "Estimating the Earth's outgoing longwave radiation measured from a moon-based platform," *Remote Sens.*, vol. 13, no. 11, 2021, Art. no. 2201.
- [36] W. Duan, J. Liu, Q. Yan, H. Ruan, and S. Jin, "The effect of spatial resolution and temporal sampling schemes on the measurement error for a Moon-based Earth radiation observatory," *Remote Sens.*, vol. 13, no. 21, 2021, Art. no. 4432.
- [37] J. Wu et al., "The influence of anisotropic surface reflection on Earth's outgoing shortwave radiance in the lunar direction," *Remote Sens.*, vol. 14, no. 4, 2022, Art. no. 887.
- [38] H. Shang et al., "Simulation of Earth's outward radiative flux and its radiance in moon-based view," *Remote Sens.*, vol. 13, no. 13, 2021, Art. no. 2535.
- [39] H. Ye, W. Zheng, H. Guo, and G. Liu, "Effects of ellipsoidal Earth model on estimating the sensitivity of moon-based outgoing longwave radiation measurements," *IEEE Geosci. Remote Sens. Lett.*, vol. 19, Jun., 2021, Art. no. 7002205.
- [40] W. Duan and S. Jin, "An improved methodology for quantifying pixel-scale entrance pupil irradiance of a Moon-based Earth radiation observatory," *IEEE ISPRS J. Photogrammetry Remote Sens.*, vol. 183, pp. 389–402, Dec., 2021.



**Jing Huang** was born in Luohe, China, in 1996. She received the graduation degree in geoinformatics from the China University of Geosciences, Wuhan, China, in 2018. He is currently working toward the Ph.D. degree in cartography and geographical information system from the Aerospace Information Research Institute, Chinese Academy of Sciences, Beijing, China and the University of Chinese Academy of Sciences, Beijing, China.

She has published two peer-reviewed journal articles related to Moon-based earth observations, which is also her research interest. Her current research interest includes Moon-based earth outgoing radiation monitoring.



**Huadong Guo** (Member, IEEE) received the graduation degree from the Geology Department, Nanjing University, Nanjing, China, in 1977 and the M.Sc. degree in cartography and geographical information system from the Graduate University of the Chinese Academy of Science (CAS), Beijing, China, in 1981.

He is the Academician of the Chinese Academy of Sciences, the foreign Academician of the Russian Academy of Sciences, Moscow, Russia, the foreign Academicians of the Finland Academy of Science and Humanities, Finland, the Academicians of the developing countries Academy of Sciences, and the Academician of the International Academy of Sciences of Eurasia.

He was the project leader of more than ten key programs related to earth observation and is the Principal Investigator for SIR-C/X-SAR, JERS-1 SAR, ERS-1/2 SAR, Radarsat-1/2, Envisat, SRTM, and ALOS programs. He has authored or coauthored more than 200 SCI index papers and 16 books.

Prof. Guo was the recipient of three national awards on science and technology, and nine awards by the Chinese Academy of Sciences. He is the President of the International Digital Earth Society, the Chairman of the International Environmental Remote Sensing Committee, the Member of the Expert Group of the United Nations Technical Promotion Mechanism for Sustainable Development Goals (SDGs), the Director of the International Centre for Space Technology for Natural and Cultural Heritage of UNESCO, Editor of *International Journal of Digital Earth* and *International Journal of Big Earth Data*.



**Guang Liu** received the B.S. and M.S. degrees in physics from Tsinghua University, Beijing, China, in 1999 and 2002, respectively, and the Ph.D. degree in cartography and geographical information system from the Institute of Remote Sensing Applications, Chinese Academy of Sciences (CAS), Beijing, China, in 2008.

From 2006 to 2007, he visited the Mathematical Geodesy and Positioning, Delft University of Technology, Delft, The Netherlands, as a Guest Researcher and worked on the time series analysis of phased array

type I-band synthetic aperture radar (PALSAR) data. He is currently a Professor with the Aerospace Information Research Institute, CAS. He is a Principal Investigator of Key Program of National Natural Science Foundation of China, focused on the frontier research of the Lunar-based earth observation platform. He has published over 30 lead-authored and 35 coauthored peer-reviewed journal articles. His research interests include the Moon-based earth observation conceptual studies, and the feasibility and potential applications of InSAR time series analysis especially in mountain area such as glacier change and landslide studies.



**Hanlin Ye** received the Ph.D. degree in cartography and geographical information system from University of Chinese Academy of Sciences, Beijing, China, in 2019.

Since 2015, he has been a part of the major program of The National Natural Science Foundation of China "Moon-based observation research of earth macroscopic scientific phenomena." He has authored or coauthored ten peer-reviewed journal articles related to the topic of Moon-based earth observations. His research interests include the earth's outgoing radiation

monitoring, the Moon-based earth observation conceptual studies, particularly the potential applications in the field of earth's outgoing radiation monitoring.